Bioenergetic characterization of a shallow-sea hydrothermal vent system: Milos Island, Greece

Guang-Sin Lu[1], Douglas E. LaRowe[1], David A. Fike[2], Gregory K. Druschel[3], William P. Gilhooly, III[3], Roy E. Price[4], Jan P. Amend[1,5]*

1 Department of Earth Sciences, University of Southern California, Los Angeles, California, United States of America, 2 Department of Earth and Planetary Sciences, Washington University in St. Louis, St. Louis, Missouri, United States of America, 3 Department of Earth Sciences, Indiana University Purdue University Indianapolis, Indianapolis, Indiana, United States of America, 4 School of Marine and Atmospheric Sciences, The State University of New York, Stony Brook, New York, United States of America, 5 Department of Biological Sciences, University of Southern California, Los Angeles, California, United States of America

* janamend@usc.edu

Abstract

Shallow-sea hydrothermal systems, like their deep-sea and terrestrial counterparts, can serve as relatively accessible portals into the microbial ecology of subsurface environments. In this study, we determined the chemical composition of 47 sediment porewater samples along a transect from a diffuse shallow-sea hydrothermal vent to a non-thermal background area in Paleochori Bay, Milos Island, Greece. These geochemical data were combined with thermodynamic calculations to quantify potential sources of energy that may support *in situ* chemolithotrophy. The Gibbs energies (ΔG_r) of 730 redox reactions involving 23 inorganic H-, O-, C-, N-, S-, Fe-, Mn-, and As-bearing compounds were calculated. Of these reactions, 379 were exergonic at one or more sampling locations. The greatest energy yields were from anaerobic CO oxidation with NO_2^- (-136 to -162 kJ/mol e$^-$), followed by reactions in which the electron acceptor/donor pairs were O_2/CO, NO_3^-/CO, and NO_2^-/H_2S. When expressed as energy densities (where the concentration of the limiting reactant is taken into account), a different set of redox reactions are the most exergonic: in sediments affected by hydrothermal input, sulfide oxidation with a range of electron acceptors or nitrite reduction with different electron donors provide 85~245 J per kg of sediment, whereas in sediments less affected or unaffected by hydrothermal input, various S^0 oxidation reactions and aerobic respiration reactions with several different electron donors are most energy-yielding (80~95 J per kg of sediment). A model that considers seawater mixing with hydrothermal fluids revealed that there is up to ~50 times more energy available for microorganisms that can use S^0 or H_2S as electron donors and NO_2^- or O_2 as electron acceptors compared to other reactions. In addition to revealing likely metabolic pathways in the near-surface and subsurface mixing zones, thermodynamic calculations like these can help guide novel microbial cultivation efforts to isolate new species.

Introduction

Hydrothermal systems are prevalent in tectonically active settings, including plate boundaries and hot spots [1–5]. They are commonly categorized by location and water depth into (1) terrestrial, (2) deep-sea (water depth >200 m), and (3) shallow-sea (water depth <200 m) [4, 6, 7]. Due to their accessibility, terrestrial hydrothermal systems (often synonymous with geothermal springs) were the first to be explored [1, 3, 7]. Since the discovery in 1977 of the first deep-sea hydrothermal systems near the Galápagos Islands [8], ~700 hydrothermal vents (with 644 confirmed or inferred to be active) have been reported along the ~60,000 km-long ocean ridge system as well as in back-arc basins in every ocean basin (InterRidge Vents Database: https://vents-data.interridge.org/). Approximately 70 active shallow-sea hydrothermal vent systems have also been identified [6, 9, 10]. Compared to their deep-sea counterparts, they occur in more diverse tectonically active settings, including near submarine volcanoes, island and intra-oceanic arcs, ridge environments, intraplate oceanic volcanoes, continental margins, and rift basins. Corresponding to their setting, the source of water for these systems can be a mixture of meteoric, magmatic, groundwater, and/or seawater. Unlike deep-sea systems, their location in the euphotic zone allows for photosynthetic activity as well [6, 9, 10]. Perhaps because they are influenced by and transitional between terrestrial and off-shore geologic environments, shallow-sea hydrothermal vent systems are typically complex and dynamic, establishing unique microbial ecosystems.

The microbial ecology and physiology in and around hydrothermal systems—terrestrial and marine—have been studied for several decades, but the factors that control community composition and metabolic function remain elusive. What is known, however, is that these systems contain the necessary ingredients for life—carbon sources, chemical energy from thermodynamic disequilibrium, mineral surfaces, and compositional gradients. Because all biological processes, including anabolism, catabolism, growth, development, and reproduction, are dependent on energy transformations [11–17], quantifying the amounts of energy associated with biological processes guides our understanding of ecosystem dynamics. The amount of energy that microorganisms can gain by catalyzing catabolic reactions in their environment can be quantified by calculating the Gibbs energy of redox reactions (ΔG_r), which depends on physicochemical variables, including temperature, pressure, pH, concentrations of products and reactants, and ionic strength. These physicochemical variables and consequently the redox reaction energy yields can vary considerably from one hydrothermal system to the next, with the structure and function of the resident microbial community closely tied to the geologic setting. We can build upon earlier studies that have shown that thermophilic archaea and bacteria in these environments can catalyze a tremendous array of redox reactions to gain energy. Many of these thermophiles are chemolithoautotrophic, i.e., they use metabolic strategies that rely only on inorganic compounds as sources of energy and carbon [14, 18–22]. In fact, a number of studies have quantified the energetic potentials in terrestrial geothermal springs [23–29], deep-sea hydrothermal systems [30–35], and shallow-sea hydrothermal systems [22, 36–42].

Several studies have described the geology, geochemistry and microbiology of the shallow-sea hydrothermal system at Milos [43–49], but the bioenergetic potential there has not been quantified. In this study, we quantify the energetics of 730 inorganic redox reactions in a shallow-sea hydrothermal system of Milos Island, Greece. The reactions include electron donors and acceptors of five major elements (H, C, N, O, S) and three trace elements (Fe, Mn, As) that are commonly enriched in hydrothermal fluids. The thermodynamic calculations can be used to link the energetic potential of microbial communities to molecular evidence of their identities and metabolic capacity.

Materials and methods

Field work and chemical analyses

Samples were collected in May 2014 from Paleochori Bay, Milos Island (Greece) under a permit from the Greek Ephorate of Underwater Antiquities. In this study, we investigated samples from the Saganaki diffuse vent (36˚40'24N, 24˚30'50E), located under ~12 m of water and ∼300 m offshore (Fig 1A and 1B). Milos Island is located in the South Aegean Sea and is part of the Hellenic Volcanic Arc [50, 51] (Fig 1A). The volcanic activity that is responsible for active gaseous hydrothermal venting on and around the island has occurred since the Pliocene. The field sampling, sample preservation, and analytical protocols used in this study were based
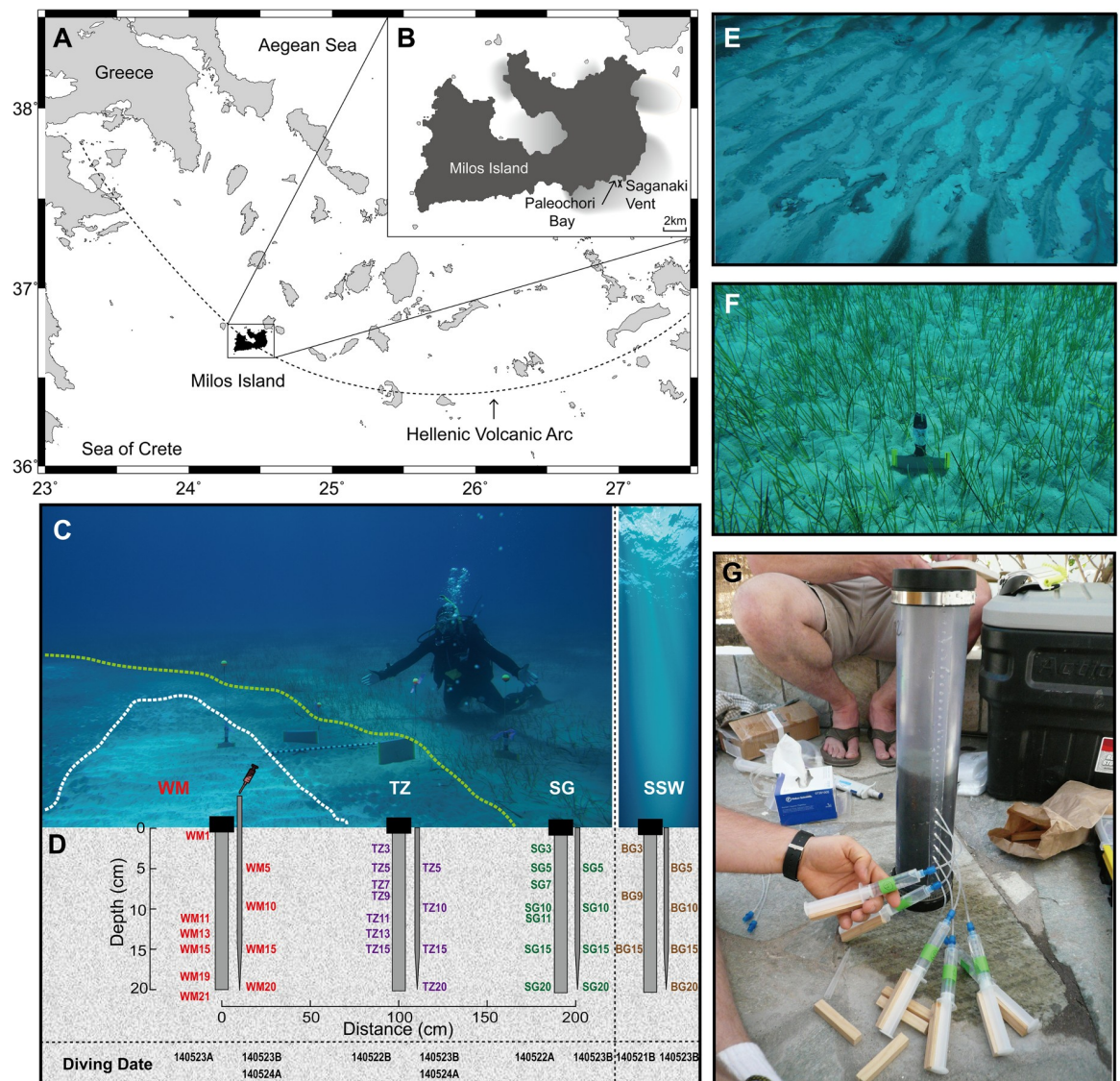
Fig 1. Site map. (A) and (B) Location of the Saganaki diffuse vent in Paleochori Bay (~300 m offshore, 12 m water depth). (C) Photograph of Saganaki showing three of the biogeographic zones: white mat (WM), transition zone (TZ), and seagrass area (SG). (D) Schematic of sampling methods (push cores and long pipettes indicating the position and depth (in cm) of samples collected for geochemistry and sequencing analysis. (E) Photograph of white mat area. (F) Photograph of seagrass area. (G) Photograph of porewater sampling from sediment cores using rhizons.

https://doi.org/10.1371/journal.pone.0234175.g001

on those described in detail elsewhere [36, 38, 47, 49, 52–54], with minor modifications for our specific field location.

A SCUBA diving team measured *in situ* temperatures and collected fluid (via long pipette) and gas samples from the vent system. Large volumes of fluids with coarse resolution were collected under water through long pipette tips inserted directly into the sediments (~5 cm depth interval, from 5 to 20 cm deep) and attached to 60-mL syringes (Fig 1C and 1D). Free gas samples were obtained with a stainless-steel funnel placed on sites with visible gas bubbles. Glass serum bottles with blue rubber stoppers were filled with seawater before the dive and then connected to the top of the funnel. Once the gas completely replaced the seawater and flushed through for approximately 5 minutes, the valves were closed. Sediment cores (in polycarbonate tubes) were collected and sealed underwater with rubber caps. Sites included the center of a white mat (WM), through a transition zone (TZ) and a sea grass-covered region (SG), ending in a background area (BG) (Fig 1C, 1D, 1E, and 1F).

On shore, waters were carefully transferred into pre-cleaned serum bottles and capped without trapping any air (for dissolved gas analyses) or filtered (0.2 μm) and stored as described below for other analyses. Rhizons (0.2 μm filter) were inserted into pre-drilled holes of the polycarbonate tubes at 2 cm intervals from 0 to 20 cm to obtain high-resolution samples while avoiding fluid reflux from different depths (Fig 1G). All porefluids were analyzed for pH and then subsampled and treated for later geochemical measurements. The subsamples were stored in acid-washed polypropylene bottles for organic acid and anion analyses; acidified with 2% ultrapure HNO_3 in acid-washed plastic bottles for cation analyses; acidified with 2% HCl and kept in opaque acid-washed glass bottles for arsenic speciation; fixed with zinc acetate solution for sulfide analysis; and stored in acid-washed and combusted glass vials for dissolved organic carbon (DOC) and total dissolved nitrogen (TDN) analyses.

Samples for major anions (F^-, Cl^-, Br^-, SO_4^{2-}, NO_3^-, NO_2^-, PO_4^{3-}) were analyzed on a Metrohm 850 Professional ion chromatograph (IC). Major and minor cation (Li^+, Na^+, K^+, Mg^{2+}, Ca^{2+}, Sr^{2+}, Ba^{2+}, Si^{2+}, B^{3+}, Mn^{2+}, Fe^{2+}) samples were measured on a Perkin-Elmer Optima inductively coupled plasma atomic emission spectrometer (ICP-OES). Samples set aside for arsenic (As^{3+}, As^{5+}, monomethylarsonic acid (MMA), and dimethylarsinic acid (DMA)) concentrations were analyzed on a Dionex ion chromatograph coupled to a PSAnalytical atomic fluorescence spectrometer (IC-AFS). Sulfide samples were analyzed by spectrophotometry with the Cline method. Dissolved organic carbon (DOC) was determined using high-temperature combustion on a Shimadzu Total Organic Carbon Analyzer (TOC-V) at the DOM Analytical Lab, Marine Science Institute, University of California-Santa Barbara. The dissolved gases were extracted from water samples after equilibrium was attained between the water sample and a known volume of high purity argon, which was injected directly into the serum bottles. Both free and dissolved gases were measured with a Shimadzu GC-2014ATF headspace gas chromatograph equipped with TCD and FID detectors.

Thermodynamic modeling

The maximum amount of available energy from potential chemolithoautotrophic reactions at the temperature, pressure, and chemical composition of interest is given by the Gibbs energy (ΔG_r). Values of ΔG_r were calculated using the relation

$$\Delta G_r = \Delta G_r^0 + RTlnQ_r \qquad (1)$$

where ΔG_r^0 denotes the standard state Gibbs energy of reaction, R designates the universal gas constant, T stands for the temperature in Kelvin, and Q_r represents the reaction quotient. Values ΔG_r^0 were calculated at the temperatures and pressures of interest with the revised-

Helgeson-Kirkham-Flowers (HKF) [55–57] equations of state using OrganoBioGeoTherm (OBIGT)—which is a user-friendly version of the SCUPCRT92 software package [58]—and thermodynamic data from several sources [56, 59–65].

Values of Q_r were calculated with

$$Q_r = \prod a_i^{\nu_{i,r}} \qquad (2)$$

where a_i designates the activity of the ith species raised to its stoichiometric reaction coefficient $\nu_{i,r}$, in the rth reaction, which is positive for products and negative for reactants. The activities of pure minerals (pyrite (FeS_2), elemental sulfur (S^0), magnetite (Fe_3O_4), hematite (Fe_2O_3), goethite ($FeOOH$), ferrihydrite ($FeOOH$), and pyrolusite (MnO_2)) and water are taken to be unity ($a_i = 1$). Molalities of the ith species in solution (m_i) were obtained as noted above, and converted into activities using the individual activity coefficient of the ith species, γ_i:

$$a_i = m_i \gamma_i \qquad (3)$$

Values of activity coefficients were calculated using the program SPEC8 (Geochemist's Workbench Version 11, Aqueous Solutions LLC) employing the extended Debye-Hückel equation [66]. Aqueous activities of dissolved gases (H_2, CH_4, O_2, CO, CO_2, CH_4) were calculated from free gas composition data assuming equilibrium. The reactions under consideration include numerous potential electron acceptors (O_2, CO, CO_2, HCO_3^-, N_2, NO_2^-, NO_3^-, pyrite, elemental sulfur, magnetite, hematite, goethite, ferrihydrite, pyrolusite, $H_2AsO_4^-$,) and donors (H_2, CH_4, CO, NH_4^+, N_2, NO_2^-, H_2S, pyrite, elemental sulfur, magnetite, Mn^{2+}, H_3AsO_3,) (S1 Table). To permit us to evaluate the energetics of both the forward and reverse direction of every reaction, we also include H_2O as a potential electron acceptor (where H in H_2O can be reduced) and electron donor (where O in H_2O can be oxidized).

To facilitate comparisons among reactions, values of ΔG_r were normalized to the number of moles of electrons transferred in the redox process [14]. In order to scale energy availability to the limiting reactant, the Gibbs energies are also presented in terms of energy densities, E_r [67]. To normalize the E_r on a 'per kg of venting fluid' and on a 'per kg of sediment' basis, values of ΔG_r were multiplied by the concentration of the limiting reactant in the fluid. The energy densities in fluid (E_{fluid}) were calculated by

$$E_{fluid} = \left| \frac{\Delta G_r}{V_i} \right| [m_{i,\,fluid}] \qquad (4)$$

where $[m_{i,fluid}]$ refers to the molal concentration of the ith limiting electron donor or acceptor per kg of fluid, taking the stoichiometry of the reaction into account. The energy densities in sediment ($E_{sediment}$) were calculated with

$$E_{sediment} = \left| \frac{\Delta G_r}{V_i} \right| [m_{i,\,sediment}] \qquad (5)$$

where $[m_{i,\,sediment}]$ is the molal concentration of the ith limiting electron donor or acceptor per kg of sediment, considering the porosity of sediments and the density of grains in them (Table 1). We did not evaluate the energy densities for reactions in which solid phases serve as both electron donor and acceptor (Reactions K66-68, L38-43, N17-19, O33-38, P33-38, Q33-38, R16-20, R25-27).

Table 1. Selected sediment properties and concentrations of Fe, Mg and S in solid phases in the Milos shallow-sea hydrothermal system.

Parameter		Reference
Porosity (%)	36	[68]
Grain density (g/cm^3)	2.66	[68]
Wet density (g/cm^3)	2.07	This study
Mean composition of clay pelites (%)	6.53	[69]
Mean Fe concentration in pelites (%)	3.4	[69]
Mean Mn concentration in pelites (ppm)	1685	[69]
Total Fe in sediment (%)	0.22	This study
Total Mn in sediment (%)	0.011	This study
Total S in 1g dry sediment	10 μM	Unpublished data

Mixing model

Values of ΔG_r for all of the reactions listed in S1 Table were also calculated for different mixing ratios of end-member hydrothermal fluid (HF, also referred to as vent fluid) with seawater. The composition of the end-member HF was taken to be the average of white mat samples, and that for seawater was taken from Table 2. The activities of species that are very low in the end-member HF (e.g., oxygen) were taken to be 10^{-9}. Although the compositions of the mixed fluids are simply proportional to the ratio of end-member fluid to seawater, the temperatures of the mixed fluids (T_{mix}) are not a linear combination of the source fluids due to their differing heat capacities. These values were calculated using

$$T_{mix} = \frac{\sum_i m_i C_{pi} T_i}{\sum_i m_i C_{pi}}$$ (6)

where m_i, C_{pi}, and T_i refer to the mass, specific heat capacity, and temperature (K) of the ith fluid. Values of C_{pi} were calculated using the equations of state for water in SUPCRT92 [70, 71]. The temperature of the end-member HF was estimated by extrapolation using the [Mg] = 0 method [72, 73].

Results and discussion

Sample location and geochemistry

The 47 fluid samples from the Saganaki vent area (Fig 1B and Table 2) represent different mixing ratios and physicochemical properties of venting fluids in this system. The hottest area (up to 76.2˚C) was covered by a ~1 cm thick, fluffy, white mat (WM) (Figs 1C, 1E, 2 and Table 2). A ~1 m wide transition zone (TZ) separates a flourishing seagrass (SG) area from the diffuse venting site (Fig 1C). Fifteen samples were taken from WM, 15 from TZ, 9 from SG, 7 from background sediment (BG) and 1 from surface seawater (SW).

Fluid measurements (Fig 2 and Table 2) reveal a wide range of temperature (19.1–76.2˚C) and pH (4.4–7.4), as well as sharp differences in geochemistry for the five sampling regions. For example, concentrations of SO_4^{2-} (13.4–34.5 mM), Na^+ (401.2–539.2 mM), and Mg^{2+} (26.6–59.6 mM) increase as a function of distance from the diffuse vent in the WM area. In contrast, K^+ levels were almost twice as high (22.7–25.9 mM) at WM than at other sites (10.3–12.1 mM). NO_3^- concentrations were below detection (b.d., 8 μM) in all samples, but NO_2^- levels were relatively high (0.15–0.23 mM) in several samples. We note that very low nitrate levels ($<$ 0.5–3.5 μM) have previously been reported in Mediterranean surface waters, especially around

Table 2. Temperature, pH and composition of porefluids and seawater sampled at or near the Saganaki diffuse vent, Milos Island, Greece.

Date-Dive-Type-Depth(cm)	T (oC)	pH	Na+ (mM)	K+ (mM)	Mg2+ (mM)	Ca2+ (mM)	Sr2+ (µM)	Ba2+ (µM)	Fe2+ (µM)	Mn2+ (µM)	As3+ (µM)	As5+ (µM)	Cl (mM)	Br- (mM)	NO2- (mM)	NO3- (mM)	SO42- (mM)	SiO2 (mM)	H2S/HS- (µM)	DOC (µM)
White Mat																				
140523A-WM1		6.55	531.0	11.0	58.8	11.9	99.4	0.32	1.84	1.79			610.7	1.51	b.d.	b.d.	26.70	0.21	3.84	
140523A-WM5		5.37	498.9	12.4	53.8	11.9	91.3	0.75	1.91	28.31			573.7	0.72	b.d.	b.d.	25.97	2.72	324.67	
140523A-WM11	39.5	4.97	490.4	12.4	52.9	11.9	91.7	0.74	1.16	29.56	0.24	b.d.	564.0	0.72	b.d.	b.d.	24.29	2.95	1402.31	
140523A-WM13		4.89	496.6	13.5	53.0	12.6	96.6	0.67	0.34	30.75	0.23	b.d.	571.1	0.71	b.d.	b.d.	28.27	2.89	1115.29	
140523A-WM15	47.5	4.86	499.3	13.2	53.7	12.5	95.7	0.69	0.28	28.42	0.17	b.d.	574.2	0.74	b.d.	b.d.	24.07	2.90	1366.07	
140523A-WM19	53.0	5.12	477.1	12.5	51.6	11.9	91.6	0.70	0.43	27.11	0.24	b.d.	548.7	0.71	b.d.	b.d.	28.04	2.77	711.94	
140523A-WM21		4.94	471.9	11.9	51.6	11.7	90.0	0.61	0.15	24.57			542.7	0.74	b.d.	b.d.	24.46	2.70	1169.07	
140523B-WM5	51.8	4.56	401.2	25.8	26.6	15.0	115.1	1.13	93.43	78.30	0.13	0.002	461.4	0.60	0.16	b.d.	14.35	3.73		960.40
140523B-WM10	66.7	4.44	402.3	25.9	26.7	14.9	115.1	1.23	95.65	73.63	0.23	0.003	462.6	0.62	0.17	b.d.	13.73	3.70		1133.67
140523B-WM15	72.6	4.66	412.1	22.7	31.9	13.4	107.1	1.10	69.98	51.06	0.44	0.010	473.9	0.66	0.18	b.d.	17.38	3.25		1043.87
140523B-WM20	76.2	4.59	414.2	23.7	30.9	14.0	110.7	1.17	65.50	53.99	0.61	0.003	476.3	0.67	0.15	b.d.	13.39	3.37		1325.41
140524A-WM5	38.9	4.71	411.3	10.4	44.6	8.1	66.0	0.60	6.99	44.80	0.32	0.002	473.0	0.60	0.16	b.d.	23.17	3.05	991.53	1036.98
140524A-WM10	57.6	4.70	410.7	10.1	44.5	8.1	66.2	0.68	6.09	43.14	0.28	0.001	472.3	0.62	0.16	b.d.	22.83	3.02	838.92	1086.84
140524A-WM15	66.5	4.68	409.6	10.2	44.4	8.1	65.9	0.71	5.80	42.97	0.27	0.001	471.0	0.66	0.18	b.d.	21.37	3.03	1037.74	1203.65
140524A-WM20	71.3	4.67	413.6	10.0	44.9	8.2	66.9	0.81	7.07	40.25	0.24	0.001	475.6	0.67	0.17	b.d.	20.81	2.94	1631.73	1198.96
Transition Zone																				
140522B-TZ3	19.1	5.56	522.4	10.7	58.3	11.7	98.4	0.24	69.13	3.22	0.94	b.d.	600.8	0.90	b.d.	b.d.	33.00	0.72	11.02	
140522B-TZ5	23.0	5.64	520.5	10.6	58.1	11.7	98.1	0.30	50.58	3.32	0.37	b.d.	598.6	0.75	b.d.	b.d.	32.36	1.04	469.85	
140522B-TZ7	25.0	5.27	518.4	10.6	58.0	11.6	97.7	0.34	11.17	3.21	0.85	b.d.	596.2	0.79	b.d.	b.d.	34.45	1.21	823.59	
140522B-TZ9	27.0	5.21	521.1	10.6	58.4	11.7	99.2	0.36	2.77	3.32	0.66	b.d.	599.3	0.77	b.d.	b.d.	33.17	1.32	275.05	
140522B-TZ11	28.0	5.19	516.2	10.4	57.9	11.6	97.9	0.35	0.37	3.42	0.84	b.d.	593.6	0.77	b.d.	b.d.	33.00	1.36	729.99	
140522B-TZ13	30.0	5.12	526.1	10.6	59.0	11.8	99.8	0.44	0.99	3.01	1.40	0.001	605.0	0.74	b.d.	b.d.	32.37	1.29	1228.93	
140522B-TZ15	31.0	5.12	524.3	10.6	58.8	11.8	99.5	0.38	0.22	3.73	0.47	b.d.	602.9	0.74	b.d.	b.d.	31.57	1.40	1162.86	
140523B-TZ5	23.1	5.15	518.4	10.5	57.6	12.1	96.6	0.39	8.10	7.91	0.06	0.001	596.2	0.77	0.22	b.d.	28.77	1.59		1122.10
140523B-TZI10	27.2	4.88	528.0	10.8	58.4	12.4	99.2	0.41	0.28	9.46	0.04	b.d.	607.2	0.78	0.23	b.d.	28.55	1.88		1168.38
140523B-TZI15	31.0	4.87	518.2	10.6	57.3	12.2	97.4	0.40	b.d.	9.25	0.02	b.d.	595.9	0.77	0.21	b.d.	25.97	1.86		1233.12
140523B-TZ20	34.2	4.76	512.3	10.5	56.7	12.1	96.0	0.39	b.d.	9.32	0.03	b.d.	589.1	0.77	0.21	b.d.	29.50	1.90		1190.97
140524A-TZ5	21.9	5.00	513.5	10.4	57.3	11.6	96.1	0.25	9.20	2.38	0.10	0.001	590.5	0.77	0.21	b.d.	27.99	0.78	896.83	1287.39
140524A-TZI10	23.9	4.77	512.2	10.5	57.0	11.6	96.8	0.33	2.36	2.67	0.08	0.001	589.0	0.78	0.21	b.d.	26.87	1.22	825.40	1133.40
140524A-TZI15	25.9	4.79	503.9	10.3	56.1	11.4	96.0	0.34	4.16	2.45	0.11	0.001	579.5	0.77	0.23	b.d.	28.66	1.26	1619.58	1063.70
140524A-TZ20	28.5	4.80	511.2	10.4	56.8	11.6	97.1	0.36	2.03	2.39	0.18	0.002	587.9	0.77	0.21	b.d.	24.74	1.30	1081.85	1188.49
Seagrass																				
140522A-SG3	19.1	7.04	530.8	11.7	59.4	11.6	98.6	0.14	23.52	1.08	0.50	0.058	610.4	0.93	b.d.	b.d.	26.47	0.02	0.28	
140522A-SG5	19.1	7.12	525.7	11.6	58.9	11.5	98.1	0.20	11.21	0.82			604.6	0.87	b.d.	b.d.	25.97	0.02	1.27	
140522A-SG7	19.1		538.3	12.1	59.4	11.7	99.5	0.16	11.05	1.12	0.66	0.053	619.0	0.91	b.d.	b.d.	25.41	0.02	0.21	
140522A-SG11	19.1	7.13	538.1	12.1	59.5	11.7	99.0	0.18	12.01	0.91	0.41	0.077	618.8	0.94	b.d.	b.d.	26.31	0.03	0.42	
140522A-SG15	19.1	7.05	535.6	11.9	59.3	11.7	99.3	0.19	11.84	0.86	1.16	0.135	615.9	0.01	b.d.	b.d.	25.58	0.03	0.78	
140523B-SG5	19.8	6.80	534.3	11.8	59.1	11.6	98.7	0.13	14.38	0.83	0.49	0.001	614.4	0.87	0.21	b.d.	26.36	0.03	1.20	1219.35

(Continued)

Table 2. (Continued)

Date-Dive-Type-Depth(cm)	T	pH	Na$^+$	K$^+$	Mg^{2+}	Ca^{2+}	Sr^{2+}	Ba^{2+}	Fe^{2+}	Mn^{2+}	As^{3+}	As^{5+}	Cl$^-$	Br$^-$	NO$_2^-$	NO$_3^-$	SO$_4^{2-}$	SiO$_2$	H$_2$S/HS$^-$	DOC
	oC		mM	mM	mM	mM	µM	µM	µM	µM	µM	µM	mM	mM	mM	mM	mM	mM	µM	µM
140523B-SG10	20.3	6.54	534.9	11.8	59.3	11.6	98.5	0.15	17.02	1.17	0.41	0.001	615.1	0.98	0.23	b.d.	28.04	0.04	0.69	1210.81
140523B-SG15	20.8	6.84	530.1	11.7	58.7	11.5	98.2	0.16	20.56	1.36	0.41	0.017	609.6	0.86	0.23	b.d.	28.27	0.05	2.84	1160.12
140523B-SG20	21.3	6.93	536.4	11.9	59.3	11.7	98.8	0.18	21.20	1.51	0.45	0.011	616.9	0.90	0.20	b.d.	25.69	0.05	1.89	1323.48
Background																				
140521B-BG3	19.1	6.34	524.8	11.4	58.7	11.4	97.1	0.08	b.d.	b.d.	0.10	b.d.	603.5	0.90	b.d.	b.d.	32.31	b.d.	0.21	481.33
140521B-BG9	19.1	6.75	527.4	11.5	59.1	11.5	98.2	0.13	2.28	0.07	0.01	b.d.	606.5	0.84	b.d.	b.d.	29.81	0.02	b.d.	773.76
140521B-BG15	19.2	6.64	528.4	11.5	59.1	11.5	98.6	0.15	14.74	0.39	0.17	b.d.	607.7	0.90	b.d.	b.d.	32.05	0.04	1.41	649.64
140523B-BG5	19.2	6.88	531.4	12.0	58.6	11.6	98.6	0.12	0.83	2.07	0.21	0.002	611.1	0.91	0.21	b.d.	23.39	0.05	0.19	1198.69
140523B-BG10	19.1	6.62	529.2	11.6	58.6	11.5	97.3	0.11	b.d.	0.18	0.04	0.001	608.6	0.82	0.23	b.d.	30.14	0.01	0.32	1134.78
140523B-BG15	19.1	7.09	527.7	11.6	58.5	11.5	97.6	0.13	0.34	0.05	0.06	0.002	606.9	0.81	0.20	b.d.	21.71	0.02	0.06	1019.07
140523B-BG20	19.0	7.14	539.2	11.9	59.6	11.7	99.2	0.15	1.33	0.03	0.09	0.003	620.1	0.92	0.21	b.d.	25.75	0.03	0.26	1089.60
Seawater																				
140525A-SW	19.0	7.4	528.5	11.6	59.2	11.6	98.5	0.06	b.d.	0.2	0.1	b.d.	607.8	1.01	0.23	b.d.	28.4	0.01	0.100	528.85
Calculated Endmember																				
Average	199.41	4.12	119.98	29.56	0.00	11.57	61.04	3.75	121.82	204.17	0.79	0.01	18.09	0	0	0	0	14.73	5180.57	-

b.d. = below detection.

https://doi.org/10.1371/journal.pone.0234175.t002
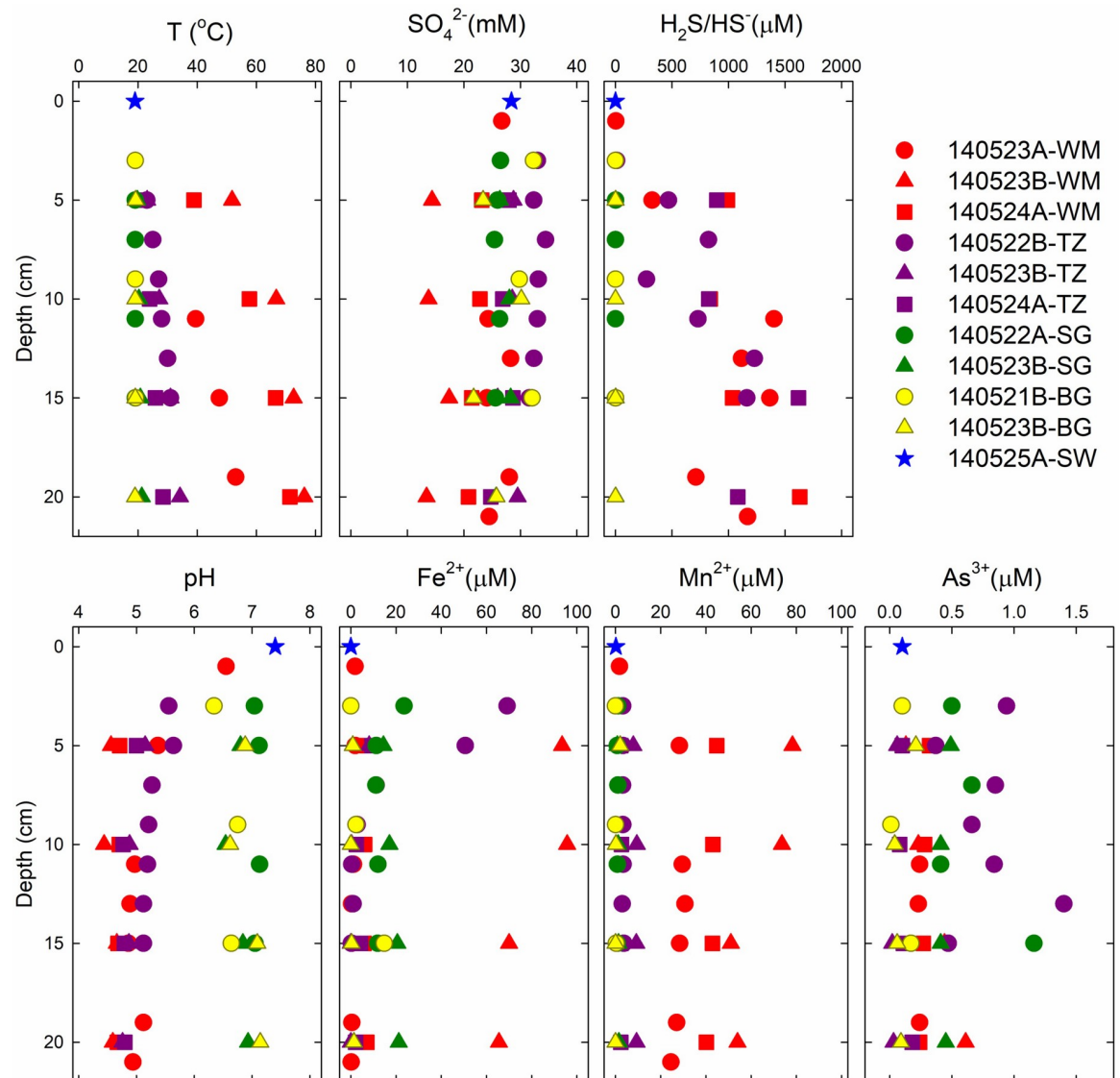
Fig 2. Geochemical profiles of temperature, pH, and selected ions. Red symbols refer to white mat (WM), purple to transition zone (TZ), green to seagrass (SG), yellow to background (BG) and blue to surface seawater (SW). Different symbols of the same color indicate different date/time of the sampling dives.

https://doi.org/10.1371/journal.pone.0234175.g002

Greece [74], and near mM concentrations of nitrite are known to occur in marine sediments [75]. Concentrations of reduced species, such as H_2S, Fe^{2+}, and Mn^{2+} range from b.d. (1 μM, 0.1 μM, and 0.04 μM, respectively) to relatively high levels (93 μM, 78 μM, and 1631 μM, respectively). Consistent with the stable and conservative nature of salinity in seawater (i.e., the principle of constant proportions), and to maintain required charge balance, concentrations of Cl^- in Table 2 were calculated from a well-established Cl^-:Na^+ ratio of 1.15 (e.g., [76]).

Porefluid energetic potential

Values of ΔG_r for the 730 reactions listed in S1 Table were calculated with Eqs (1–4) using the fluid compositions and environmental conditions given in Tables 2 and 3. Values of ΔG_r in kJ

Table 3. Dissolved and free gas composition in white mat (WM), transition zone (TZ) and background (BG) areas.

Sample	H_2	O_2	N_2	CO_2	CH_4	CO
WM Free Gas (%)	b.d.	2.72	18.00	61.36	0.299	0.025
WM Dissolved Gas at 10cm (μM)	b.d.	0.496	38.5	11.93	0.038	0.076
TZ Dissolved Gas at 5cm (μM)	b.d.	1.001	76.6	2.725	0.089	b.d.
BG (μM)	b.d.	220	456.00	2.638	b.d.	b.d.
End-member (average) (μM)	0	0	0	47.304	0.183	0.365

per mole of electron transferred are depicted in Fig 3A for the 379 reactions that are exergonic ($\Delta G_r < 0$) in at least one sampling location. The reactions are plotted from top (-162.3 kJ/mole e⁻) to bottom (near 0 kJ/mole e⁻) in order of the average energy yield at all 47 sampling sites. It can clearly be seen that for most reactions, the energy yields vary by 20–50 kJ/mol e⁻ across the different locations and sample depths; in a number of examples, especially reactions with iron (e.g. L34: $Fe^{2+}/S^{0,}$ and N16: H_2S/Fe_3O_4), the range approaches and even exceeds 80 kJ/mol e⁻. Reactions with nitrite (purple bar) and oxygen (light grey bar) as electron acceptors and with CO as electron donor are the most exergonic, with the top 10 reactions (electron donor/acceptor) being CO/NO_2^- (reaction H13, -162.3 kJ/mole e⁻), CO/NO_2^- (H14, -151.4 kJ/mole e⁻), CO/O_2 (B5, -147.9 kJ/mole e⁻), CO/NO_3^- (I18, -139.9 kJ/mole e⁻), CO/O_2 (B6, -142.6 kJ/mole e⁻), CO/MnO_2 (R5, -140.9 kJ/mole e⁻), H_2S/NO_2^- (H19, -136.0 kJ/mole e⁻), CO/NO_3^- (I19, -131.0 kJ/mole e⁻), CO/MnO_2 (R6, -130.7 kJ/mole e⁻), $CO/FeOOH_{Fer}$ (Q13, -124.9 kJ/mole e⁻) (Fig 3A).

In Fig 3B, energy yields are plotted as energy densities (E_{fluid}). Again, the range of energy yields across sites and sample depths vary tremendously, often exceeding 6 orders of magnitude in J/kg H_2O. This broad range is due to the rapid dilution of hydrothermal fluid with seawater, whereby the concentrations of some key redox species change by 2–3 orders of magnitude over short distances (Table 2). For example, the concentration of Mn in WM (28.31–78.30 μM) is 150–400 times that in seawater, and therefore E_{fluid} of Mn-redox reactions point to a much larger energy potential than the corresponding value of ΔG_r would indicate. In addition, one of the consequences of setting the activities of pure minerals to 1.0 means that energy densities of reactions involving hematite, goethite, ferrihydrite, pyrolusite, pyrite, elemental sulfur, and magnetite are high (100–10,000 J/kg H_2O). Finally, we note that the most exergonic reactions in Fig 3B are not the same as those in Fig 3A. In terms of energy density, the oxidation of sulfide, sulfur, and ammonia are thermodynamically most favorable. A phylogenetic analysis (16S rRNA) of hydrothermal sediments at Milos showed that heterotrophs and sulfur oxidizers were among the most abundant [77]. In fact, several aerobic and anaerobic sulfur oxidizers have been isolated from Milos, including *Halothiobacillus kellyi* [78], *Stetteria hydrogenophila* [79], *Thiomicrospira sp.* Milos-T1 [80], and *Gamma Proteobacteria* Milos strain ODI4G, OBII5, ODIII6, OBII5 [81].Values of ΔG_r and E_{fluid} for the exergonic reactions shown in Fig 3 are re-plotted as colored circles in Fig 4, but with average values for each of the five regions and classified by electron donors (Fig 4A and 4C) and electron acceptors (Fig 4B and 4D). In addition, the total average energy yields for all 47 samples are also plotted (black squares). In terms of ΔG_r, reactions with O_2 as the electron acceptor supplied the most energy, followed by reactions with NO_3^-, NO_2^-, and MnO_2, and then reactions with iron minerals, S^0, As^V, SO_4^{2-}, and inorganic carbon. In units of energy density (E_{fluid}), reactions with ammonia and sulfide as electron donors are the most exergonic, especially in the WM and TZ regions (Fig 4C). When color-coded by electron acceptor (Fig 4D), we note that values of E_{fluid} are generally highest (with some exceptions) in the WM region, followed by the TZ, SG, BG, and SW.
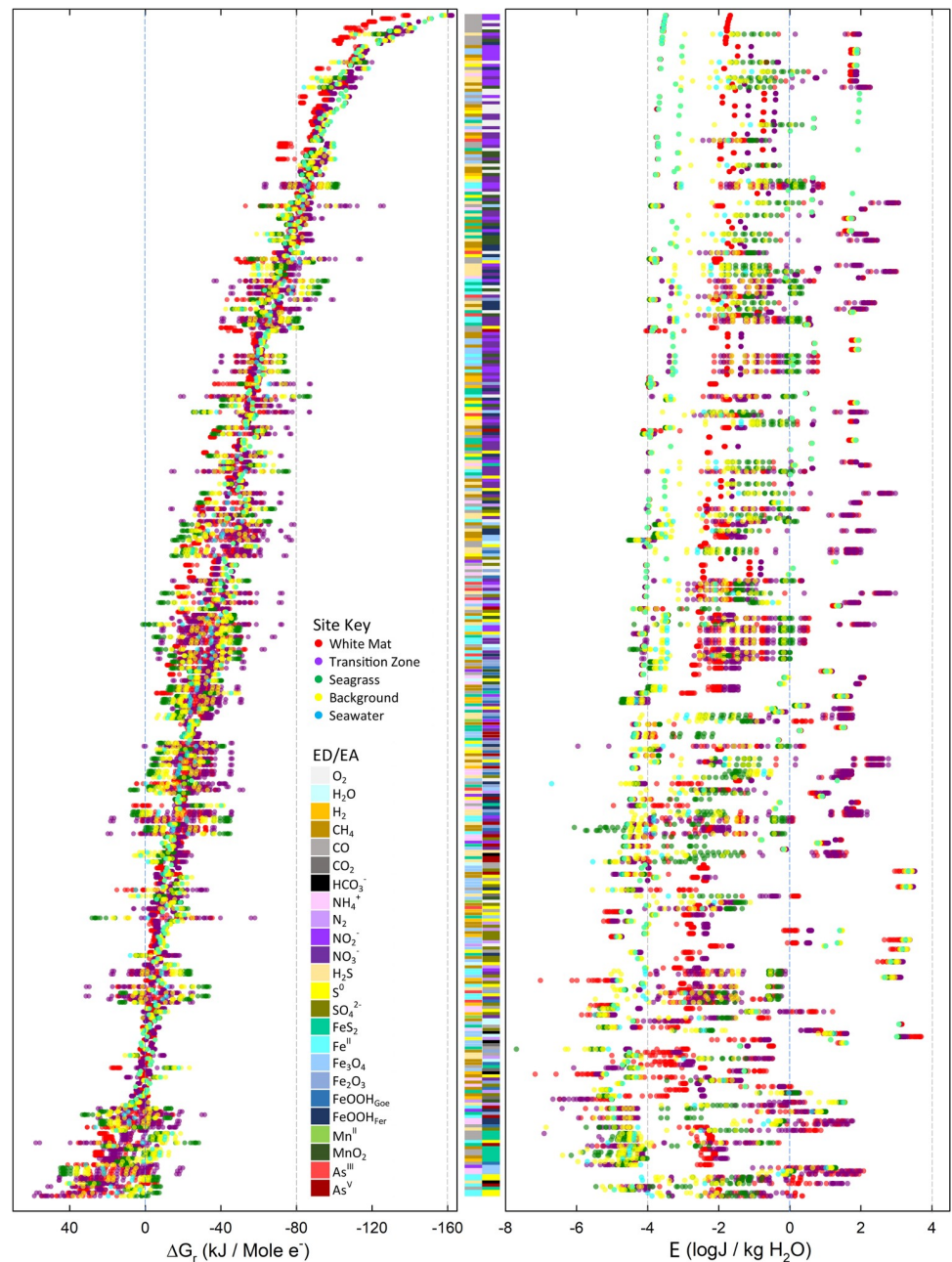
Fig 3. Overall Gibbs energy yields of the catabolic reactions considered in this study. Circles refer to values of ΔG_r of the 379 exergonic reactions shown in S2 Table at individual sample sites in units of kJ/mol e⁻ (A) and J/kg fluid (B). The colors of the circles encode for the five biogeographic regions (see key). The colored bars in the middle of the two panels refer to the identities of electron acceptors and donors in the reactions as noted in the key. The reactions are ordered from most exergonic at the top to least exergonic at the bottom, based on the averages of ΔG_r values from all samples.

See LaRowe and Amend (2019) for a discussion on reaction energetics in molal versus density units [82]. This difference can best be seen in reactions with CO, where energy values are -132 to -162 kJ/mol e⁻, but only 1.7 to 3.5 J/kg H_2O (e.g. reaction H13). Similarly, for the oxidation of methane, carbon monoxide, and ammonium, values of the energy densities are more
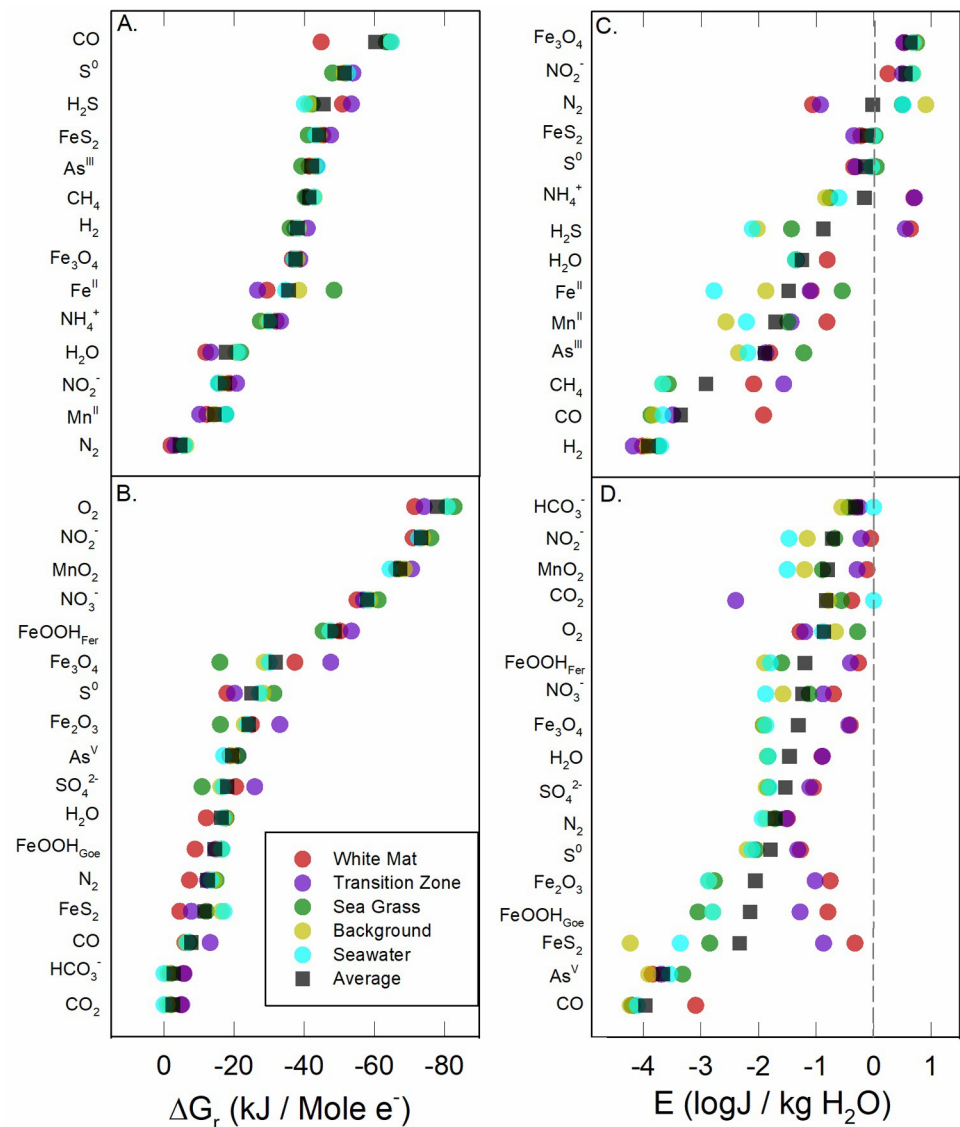
Fig 4. Average Gibbs energy yields of exergonic reactions. Average values of ΔG_r (panels A and B, in kJ/mol e⁻) and E_{fluid} (panels C and D, in J/kg H_2O) grouped by electron donors (panels A and C) and electron acceptors (panels B and D) for the five biogeographic regions considered in this study.

exergonic than the per-electron counterparts reveal, particularly in the WM and TZ regions. Because the energy densities of sulfide oxidation are so variable, it is likely that the importance of this process is highly localized, with notable potential in the more hydrothermally influenced areas (WM, TZ). Energy densities for iron, manganese, and arsenite oxidation reactions are also scattered, while those for the oxidation of elemental sulfur, pyrite and magnetite show no clear trends. Energy densities for the WM and TZ regions appearing on the right hand (i.e., more exergonic) side of Fig 4D indicates that chemolithotrophic primary production has a positive correlation with temperature, or hydrothermal source.

Similar studies of redox reaction energetics for putative chemotrophic metabolisms have been carried out for geochemically diverse hot springs in Yellowstone National Park [26], shallow-sea hydrothermal systems in the Aeolian Islands (Italy) [22, 38] and the continental

subsurface at the Sanford Underground Research Facility (SURF) in South Dakota (USA) [83]. Analogous to the present study at Milos, those communications concluded that reactions with energy yields >100 kJ/mol e$^-$ are rare and involve O_2 or NO_3^-/NO_2^- as electron acceptors. It should be noted that the maximum yields in the Milos system are at ~160 kJ/mol e$^-$, while those in the Aeolian Islands are ~120 kJ/mol e$^-$, in Yellowstone hot springs are ~110 kJ/mol e$^-$, and at SURF are ~100 kJ/mol e$^-$. Nine of the most exergonic reactions at Milos are aerobic or anaerobic carbon monoxide oxidation. We note two reasons for the higher ΔG_r yields at Milos than at other sites: First, CO and NO_2^- have large and opposite redox potentials, which tends to lead to large Gibbs energies of reaction. Second, we measured and considered a larger range of redox sensitive species than most other studies, which rarely include CO and NO_2^- because they decay quickly, or their concentrations are below detection limits.

This set of investigations also demonstrated that in a number of examples, changes in chemical composition—with pH being a major driver—can 'flip' a reaction from exergonic to endergonic. In other words, the forward reaction may serve as a putative metabolism in some environments, while the reverse direction could do so at very different geochemical conditions. Similarities among these different studies are also observed when energy densities are considered. (Note that studies focused on the shallow-sea vents at Vulcano, Aeolian Islands [22] and Yellowstone hot springs [26] did not provide such results. In each case, the most exergonic reactions in terms of energy density are different from those labeled as most exergonic in ΔG_r space.

Bulk sediment energetic potential

The calculations summarized above only considered porefluids and not the solid phase minerals that can be used as energy sources. Following the same color scheme as in Fig 3, the amount of energy available per kg of sediment ($E_{sediment}$, J/kg sediment) is shown in Fig 5A (by electron donor) and 4B (by electron acceptor). The bottom panels reveal total $E_{sediment}$ for all reactions, while the middle and top panels show values of $E_{sediment}$ <1 J/kg sediment and <10 J/kg
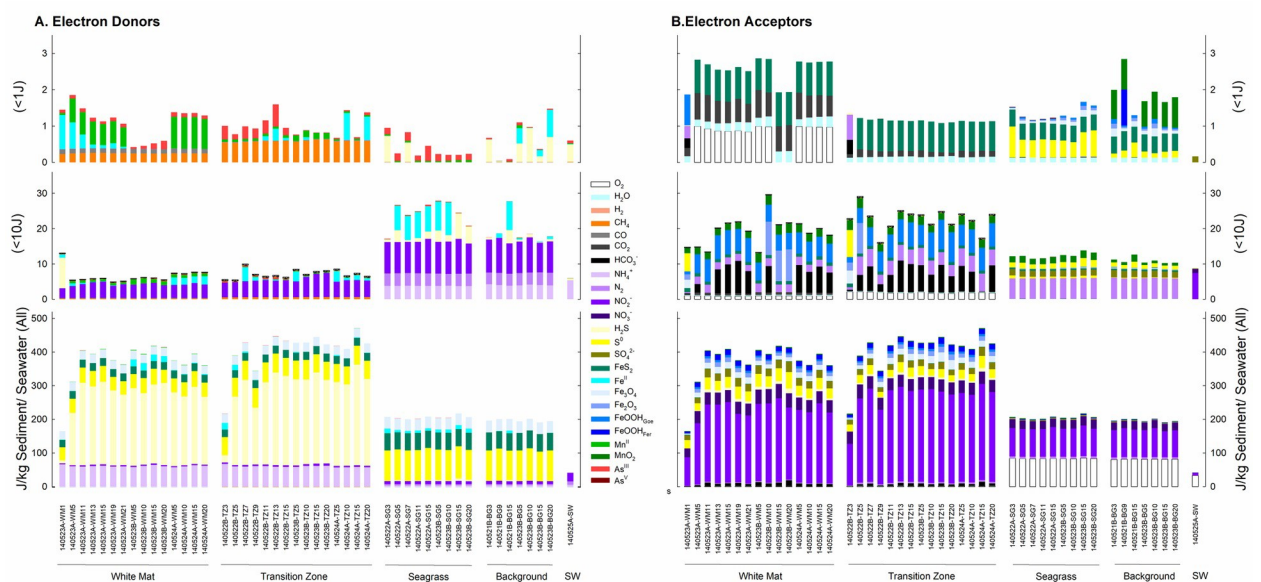
Fig 5. Energy densities at all sample locations and depths. Colored bars refer to identities of different electron donors (A) and electron acceptors (B). The upper and middle panels zoom in on reactions with low energy yields (<1 J and <10 J, respectively). The energy densities refer to either those in 1 kg sediment or 1 kg seawater. See S1 Table for details on the reactions.

https://doi.org/10.1371/journal.pone.0234175.g005

sediment, respectively. It can be seen in the bottom panel in Fig 5A that reactions with ammonia, sulfide, sulfur, magnetite, and pyrite as electron donors are the most exergonic; the bottom panel in Fig 5B shows that reactions with nitrate, nitrite, sulfur and sulfate as electron acceptors provide the most energy. These panels reveal three energy-based habitats: (1) hydrothermal-influenced sediments in the WM and TZ regions, (2) seawater-influenced sediments in the SG and BG areas and (3) surface seawater. Energy yields are similar in the WM and TZ regions, increasing with depth at both locations. Conversely, depth is not a correlating factor in the SG and BG areas. Reactions that provide relatively small amounts of energy are shown in the middle and top panels in Fig 5, with patterns of energy yields changing with the distance from the diffuse vent. Both the WM and TZ settings show increasing energy yield with sediment depth, and the dominance of aerobic respiration in seawater-influenced sediments and seawater.

From an energetics perspective, oxygen/nitrate/nitrite and sulfur/sulfide/ammonia should be the main electron acceptors and donors, respectively, to be used by chemolithotrophs at Milos (Fig 5). Based on values of Gibbs energy and elevated levels of abundance, sulfide oxidation coupled to nitrite reduction could support much of the chemolithotrophic primary production. Some evidence, though limited, is available to support this claim: three chemolithotrophic nitrate-reducing sulfate-oxidizing bacteria have been isolated from Milos [81] and isotopic evidence of microbial sulfate reduction in the TZ has been reported [84].

Mixed fluid (SW:HF) energetic potential

The estimated, weighted average temperature of the end-member HF, based on Mg content in 13 WM samples, is 199.4˚C (Fig 6A). The curve shown in Fig 6B depicts the calculated temperature of a fluid that results from titrating cold seawater (SW) into 1 kg of this end-member HF, and Fig 6C presents how the activities of major redox-active species change with the mass ratios of SW:HF from 10^3:1 to 10^{-2}:1, as well as a temperature range from 19.0 to 199.4˚C. The remaining panels in Fig 6 show how much energy is available from the 17 reactions listed in Table 4 normalized to kJ per mole electron transferred (Fig 6D), J per kg mixed fluid (Fig 6E), and J per kg vent fluid (Fig 6F), where solid lines refer to aerobic processes, dashed lines represent anaerobic processes, and the different colors identify different reactions.

Thermodynamic predictions of redox reaction energetics can change substantially when different normalization schemes are used [85, 86] For instance, when normalized to kJ per mole electron transferred ($\Delta G_r/e^-$) for the SW:HF mixing calculations, the energy yields of all reactions decreased with increasing proportion of HF (Fig 6D). When normalized per kg of mixed fluid (E_{fluid}), however, a very different picture emerges (Fig 6E); here, the reactions fall into two groups: three reactions (B14-B16) that can provide >60 J/kg mixed fluid at optimal SW:HF ratios, and the other 14 reactions where energy yields maximize at ~11 J/kg mixed fluid for one example (B24) and ~4 J/kg mixed fluid for the rest. Finally, the potential energy per kg of pure vent fluid is given in Fig 6F. In this normalization, the reactions are most exergonic at a SW:HF mixing ratio of ~100:1, corresponding to a temperature of ~20˚C. At these conditions, the energy yields from sulfide oxidation with O_2 or NO_3^- (B14, B15, I29, I30) and aerobic ammonia oxidation (B9) exceed by several orders of magnitude those of the other reactions. A similar story emerges when normalizing values of ΔG_r per kg mixed fluid and per kg vent fluid for aerobic and anaerobic sulfur/sulfide oxidation in the WM area (Fig 6E and 6F). This can be seen most clearly at temperatures <40˚C, where these reactions are 20–50 times as exergonic as the other reactions. As noted above, isotopic data also point to a dynamic sulfur cycle at Milos with microbial sulfate reduction, sulfide oxidation, and rapid recycling of sulfur intermediates that vary with location and time [47, 84].

The curves in Fig 6E (J/kg mixed fluid) and 6F (J/kg hydrothermal fluid) show how the energy densities of the reactions in Table 4 change with HF:SW ratio. The multiple y-axes are
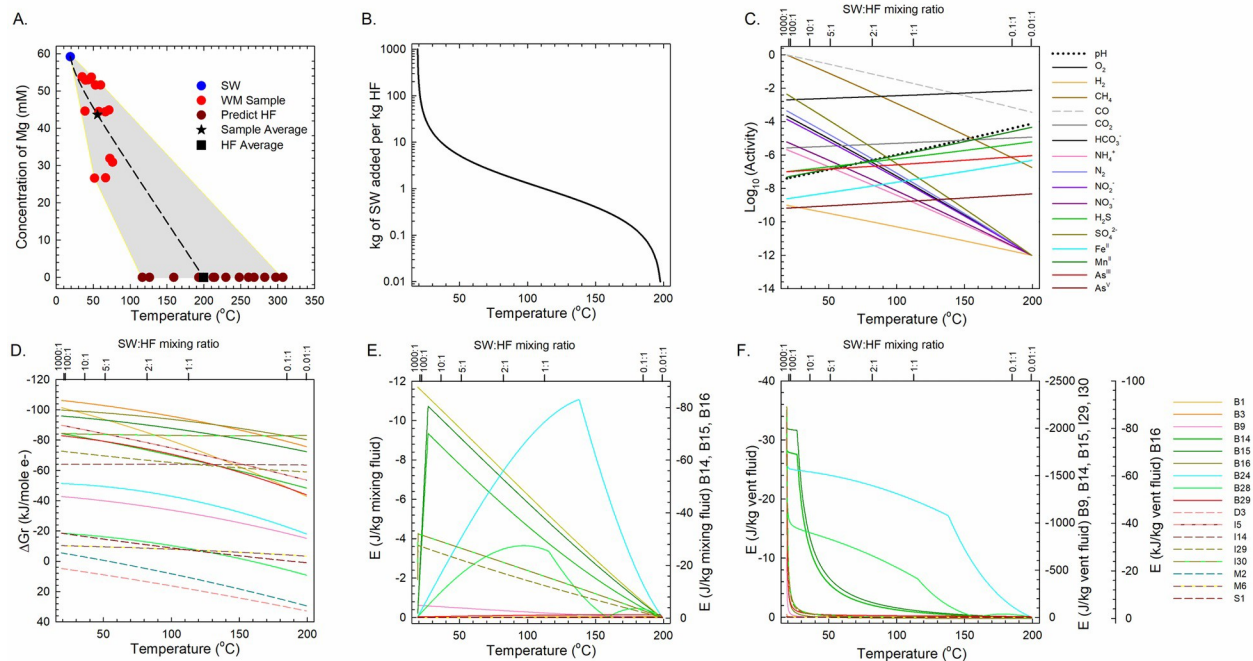
Fig 6. Temperature, composition and energetics resulting from the hydrothermal fluid-seawater mixing model. (A) Extrapolated temperature of end-member HF at [Mg] = 0 (brown circles) based on values of [Mg] in WM samples (red circles) and SW (blue circle). The temperature, composition and energetics of redox reactions resulting from fluid mixing were calculated using the average WM composition (black star) and average HF composition (black square). (B) Fluid temperature as a function of SW:HF mixing ratio. (C) Activities of redox-sensitive species as a function of temperature and SW:HF mixing ratio. Values of ΔG_r (D) and E_{fluid} (E, F) of exergonic reactions listed in Table 4. Because the results span several orders of magnitude, reactions B14, B15 and B16 have a different Y-axis scale on right side in (E); and reactions B9, B14, B15, I29, I30, and B16 refer to the two Y-axis scales on the right side in (F).

https://doi.org/10.1371/journal.pone.0234175.g006

used in Fig 6E and 6F because the results span several orders of magnitude. It can clearly be seen that as the proportion of HF decreases, the energy yields for most reactions also decrease,

Table 4. Catabolic reactions used to define metabolic groups in the analysis shown in Fig 5.

Metabolic Group	#	Reaction
Hydrogen Oxidizers	B1	$2H_2 + O_2 \rightarrow 2\,H_2O$
	I5	$5H_2 + 2NO_3^- + 2H^+ \rightarrow N_2 + 6H_2O$
Methane Oxidizers	B3	$CH_4 + 2O_2 \rightarrow CO_2 + 2H_2O$
	I14	$CH_4 + 4NO_3^- \rightarrow 4NO_2^- + CO_2 + 2H_2O$
	M6	$CH_4 + SO_4^{2-} + 2H^+ \rightarrow H_2S + CO_2 + 2H_2O$
Ammonium Oxidizers	B9	$NH_4^+ + 2\,O_2 \rightarrow NO_3^- + 2\,H^+ + H_2O$
Sulfur Oxidizers	B14	$2\,H_2S + O_2 \rightarrow 2\,S + 2\,H_2O$
	B15	$H_2S + 2\,O_2 \rightarrow SO_4^{2-} + 2\,H^+$
	B16	$2\,S + 3\,O_2 + 2\,H_2O \rightarrow 2\,SO_4^{2-} + 4\,H^+$
	I29	$5\,H_2S + 2\,NO_3^- + 2\,H^+ \rightarrow 5\,S + N_2 + 6\,H_2O$
	I30	$5\,H_2S + 8\,NO_3^- \rightarrow 5\,SO_4^{2-} + 4\,N_2 + 2\,H^+ + 4\,H_2O$
Iron Oxidizers	B24	$4\,Fe^{2+} + O_2 + 6\,H_2O \rightarrow 4\,FeOOH_{\,Ferrihydrite} + 8\,H^+$
Manganese Oxidizer	B28	$2\,Mn^{2+} + O_2 + 2\,H_2O \rightarrow 2\,MnO_{2\,Pyrolusite} + 4\,H^+$
Arsenite Oxidizers	B29	$2\,H_3AsO_3 + O_2 \rightarrow 2\,H_2AsO_4^- + 2\,H^+$
Methanogens	D3	$4H_2 + CO_2 \rightarrow CH_4 + 2H_2O$
Sulfate Reducers	M2	$4H_2 + SO_4^{2-} + 2H^+ \rightarrow H_2S + 4H_2O$
Arsenate Reducers	S1	$H_2 + H_2AsO_4^- + H^+ \rightarrow H_3AsO_3 + H_2O$

https://doi.org/10.1371/journal.pone.0234175.t004

especially when these are plotted per kg of vent fluid (Fig 6F). The kinks and inflection points in some of the curves in Fig 6E and 6F are a result of calculating the reaction energies using the concentration of the limiting electron donor or acceptor. These abrupt changes in slope correspond to points where the concentrations of the electron donors and acceptors are equal. The inflection points in Fig 6E also illustrate the temperatures at which the reactions are most exergonic. For example, the sulfur and sulfide oxidation reactions B14 and B15 have inflection points at 27˚C, above which their potential energy yields decrease. Similarly, the limiting reactant for reactions B24 and B28 changes from iron and manganese, respectively, to oxygen as temperature increases (Fig 6E). Our mixing model suggests that microbial metabolic strategies often shift with mixing ratio, and therefore temperature, a notion that is supported by other lines of evidence. Note that cell abundances of sulfur oxidizing bacteria, sulfate reducing bacteria and dissimilatory iron-reducing bacteria at Milos decrease with increasing depth and temperature [87]. Also at Milos, microbial cell numbers are highest in the shallowest sediment [77].

Conclusions

Seawater and porewater chemistries, a fluid mixing model, and thermodynamic calculations were combined to determine the energy yields of more than 700 redox reactions in fluids and sediments of a Milos Island shallow-sea hydrothermal environment. These yields were reported in several normalization schemes—in kJ per mole electrons transferred and in J per kg water or sediment—revealing potential chemolithotrophic microbial metabolisms as a function of depth and distance from a diffuse vent area. We demonstrated that in this system at Milos, analogous to other shallow-sea hydrothermal systems, hot spring environments, and the deep continental subsurface, a large number of inorganic redox reactions can be exergonic, suggesting that diverse chemolithotrophic metabolisms may be occurring simultaneously. Based on modeling of SW:HF mixed solutions in shallow sediments, we also showed that energy yields can change dramatically along the posited steep gradients in temperature, pH, and composition of redox-sensitive aqueous solutes, together with consideration of redox-sensitive minerals. In the Milos hydrothermal system, this applies to a transect from the White Mat area across the Transition Zone to the Seagrass and Background zones and into seawater. An environmental energy framework of the type provided here can help interpret biodiversity data and ecosystem function, and also guide efforts to cultivate dominant as well as important minor members of a chemolithotrophic microbial community.

Supporting information

S1 Table. Redox reactions considered in this study.
(DOCX)

S2 Table. Order of reactions shown in Fig 3 from top (1) to bottom (379).
(DOCX)

Acknowledgments

Author Contributions

Conceptualization: Guang-Sin Lu, Jan P. Amend.

Data curation: Guang-Sin Lu.

Formal analysis: Guang-Sin Lu, David A. Fike, Roy E. Price.

Funding acquisition: Douglas E. LaRowe, David A. Fike, Gregory K. Druschel, Jan P. Amend.

Investigation: David A. Fike, William P. Gilhooly, III, Roy E. Price, Jan P. Amend.

Methodology: Guang-Sin Lu, Douglas E. LaRowe.

Project administration: David A. Fike, Gregory K. Druschel, Jan P. Amend.

Resources: William P. Gilhooly, III.

Supervision: Douglas E. LaRowe, Jan P. Amend.

Writing – original draft: Guang-Sin Lu, Douglas E. LaRowe.

Writing – review & editing: Douglas E. LaRowe, David A. Fike, Gregory K. Druschel, William P. Gilhooly, III, Jan P. Amend.

References

1. Brock TD. High temperature systems. Annual review of ecology and systematics. 1970; 1(1):191–220.

2. Renner J, White D, Williams D. Hydrothermal convection systems. Assessment of geothermal resources of the United States. 7261975.

3. Rinehart JS. Geysers and geothermal energy: Springer; 1980.

4. Baker ET, German CR. On the global distribution of hydrothermal vent fields. Mid-ocean ridges. 2004:245–66.

5. Beaulieu SE. InterRidge Global Database of Active Submarine Hydrothermal Vent Fields: prepared for InterRidge, Version 3.3. World Wide Web electronic publication. Version 3.4 accessed 2018-04-28: InterRidge program; 2015.

6. Prol-Ledesma RM, Dando PR, de Ronde CEJ. Special issue on "shallow-water hydrothermal venting". Chem Geol. 2005; 224(1–3):1–4. https://doi.org/10.1016/j.chemgeo.2005.07.012

7. Waring GA, Blankenship RR. Thermal Springs of the United States and Other Countries: A Summary: US Government Printing Office; 1965.

8. Corliss JB, Dymond J, Gordon LI, Edmond JM, Herzen RPV, Ballard RD, et al. Submarine thermal springs on the galapagos rift. Science. 1979; 203(4385):1073–83. https://doi.org/10.1126/science.203.4385.1073 PubMed PMID: WOS:A1979GM37500005. PMID: 17776033

9. Tarasov VG, Gebruk AV, Mironov AN, Moskalev LI. Deep-sea and shallow-water hydrothermal vent communities: Two different phenomena? Chem Geol. 2005; 224(1–3):5–39. https://doi.org/10.1016/j.chemgeo.2005.07.021

10. Price RE, Giovannelli D. A Review of the Geochemistry and Microbiology of Marine Shallow-water Hydrothermal Vents. Reference Module in Earth Systems and Environmental Sciences. 2017.

11. Madigan MT, Bender KS, Buckley DH, Sattley WM, Stahl DA. Brock Biology of microorganisms 15th edn: Pearson; 2017. https://doi.org/10.3390/microorganisms5020034 PMID: 28635676

12. Branch GM. The biology of limpets: physical factors, energy flow, and ecological interactions. 1981.

13. Hill T. Free energy transduction in biology: the steady-state kinetic and thermodynamic formalism: Elsevier; 2012.

14. Amend JP, Shock EL. Energetics of overall metabolic reactions of thermophilic and hyperthermophilic Archaea and Bacteria. Fems Microbiology Reviews. 2001; 25(2):175–243. https://doi.org/10.1111/j.1574-6976.2001.tb00576.x PubMed PMID: WOS:000167599700002. PMID: 11250035

15. Reece JB, Urry LA, Cain ML, Wasserman SA, Minorsky PV, Jackson RB. Campbell biology: Pearson Higher Ed; 2013.

16. Larowe DE, Helgeson HC. Quantifying the energetics of metabolic reactions in diverse biogeochemical systems: electron flow and ATP synthesis. Geobiology. 2007; 5(2):153–68. https://doi.org/10.1111/j.1472-4669.2007.00099.x PubMed PMID: WOS:000247529000006.

17. Amend JP, LaRowe DE, McCollom TM, Shock EL. The energetics of organic synthesis inside and out-side the cell. Philosophical Transactions of the Royal Society B-Biological Sciences. 2013; 368(1622). https://doi.org/10.1098/rstb.2012.0255 PubMed PMID: WOS:000320105200003. PMID: 23754809

18. Jannasch H. Review lecture: The chemosynthetic support of life and the microbial diversity at deep-sea hydrothermal vents. Proceedings of the Royal Society of London B: Biological Sciences. 1985; 225 (1240):277–97.

19. Daniel RM. Modern life at high temperatures. Origins of life and evolution of the biosphere. 1992; 22 (1):33–42. https://doi.org/10.1007/bf01808017

20. Lutz RA, Kennish MJ. Ecology of deep-sea hydrothermal vent communities: A review. Reviews of Geophysics. 1993; 31(3):211–42.

21. Segerer AH, Burggraf S, Fiala G, Huber G, Huber R, Pley U, et al. Life in hot springs and hydrothermal vents. Origins of life and evolution of the biosphere. 1993; 23(1):77–90. https://doi.org/10.1007/BF01581992 PMID: 11536528

22. Amend JP, Rogers KL, Shock EL, Gurrieri S, Inguaggiato S. Energetics of chemolithoautotrophy in the hydrothermal system of Vulcano Island, southern Italy. Geobiology. 2003; 1(1):37–58. https://doi.org/10.1046/j.1472-4669.2003.00006.x PubMed PMID: WOS:000207171100005.

23. Berenguer J. Thermophile. In: Gargaud M, Amils R, Quintanilla JC, Cleaves HJ, Irvine WM, Pinti DL, et al., editors. Encyclopedia of Astrobiology. Berlin, Heidelberg: Springer Berlin Heidelberg; 2011. p. 1666–7.

24. Inskeep WP, Ackerman GG, Taylor WP, Kozubal M, Korf S, Macur RE. On the energetics of chemolithotrophy in nonequilibrium systems: case studies of geothermal springs in Yellowstone National Park. Geobiology. 2005; 3(4):297–317. https://doi.org/10.1111/j.1472-4669.2006.00059.x PubMed PMID: WOS:000207172000006.

25. Shock EL, Holland M, Meyer-Dombard D, Amend JP. Geochemical sources of energy for microbial metabolism in hydrothermal ecosystems: Obsidian Pool, Yellowstone National Park. Geothermal biology and geochemistry in Yellowstone National Park. 2005; 1:95–112.

26. Shock EL, Holland M, Meyer-Dombard D, Amend JP, Osburn GR, Fischer TP. Quantifying inorganic sources of geochemical energy in hydrothermal ecosystems, Yellowstone National Park, USA. Geochim Cosmochim Ac. 2010; 74(14):4005–43. https://doi.org/10.1016/j.gca.2009.08.036 PubMed PMID: WOS:000278977100011.

27. Spear JR, Walker JJ, McCollom TM, Pace NR. Hydrogen and bioenergetics in the Yellowstone geothermal ecosystem. PNAS. 2005; 102(7):2555–60. https://doi.org/10.1073/pnas.0409574102 PMID: 15671178

28. Spear JR, Walker JJ, Pace NR. Hydrogen and primary productivity: inference of biogeochemistry from phylogeny in a geothermal ecosystem. Geothermal Biology and Geochemistry in Yellowstone National Park. 2005:113–28.

29. Windman T, Zolotova N, Schwandner F, Shock EL. Formate as an energy source for microbial metabolism in chemosynthetic zones of hydrothermal ecosystems. Astrobiology. 2007; 7(6):873–90. https://doi.org/10.1089/ast.2007.0127 PMID: 18163868

30. Dahle H, Okland I, Thorseth IH, Pederesen RB, Steen IH. Energy landscapes shape microbial communities in hydrothermal systems on the Arctic Mid-Ocean Ridge. ISME J. 2015; 9(7):1593–606. https://doi.org/10.1038/ismej.2014.247 PubMed PMID: WOS:000356778000011. PMID: 25575309

31. McCollom TM, Shock EL. Geochemical constraints on chemolithoautotrophic metabolism by microorganisms in seafloor hydrothermal systems. Geochim Cosmochim Ac. 1997; 61(20):4375–91. https://doi.org/10.1016/s0016-7037(97)00241-x PubMed PMID: WOS:A1997YH27900012.

32. Shibuya T, Russell MJ, Takai K. Free energy distribution and hydrothermal mineral precipitation in Hadean submarine alkaline vent systems: Importance of iron redox reactions under anoxic conditions. Geochim Cosmochim Ac. 2016; 175:1–19. https://doi.org/10.1016/j.gca.2015.11.021 PubMed PMID: WOS:000369070000001.

33. Eecke HCV, Akerman NH, Huber JA, Butterfield DA, Holden JF. Growth kinetics and energetics of a deep-sea hyperthermophilic methanogen under varying environmental conditions. Env Microbiol Rep. 2013; 5(5):665–71. https://doi.org/10.1111/1758-2229.12065 PubMed PMID: WOS:000325142700005. PMID: 24115616

34. Hentscher M, Bach W. Geochemically induced shifts in catabolic energy yields explain past ecological changes of diffuse vents in the East Pacific Rise 9˚ 50'N area. Geochem T. 2012; 13(1):2.

35. McKay L, Klokman VW, Mendlovitz HP, LaRowe DE, Hoer DR, Albert D, et al. Thermal and geochemical influences on microbial biogeography in the hydrothermal sediments of Guaymas Basin, Gulf of California. Env Microbiol Rep. 2016; 8(1):150–61. https://doi.org/10.1111/1758-2229.12365 PubMed PMID: WOS:000371481100019. PMID: 26637109

36. Akerman NH, Price RE, Pichler T, Amend JP. Energy sources for chemolithotrophs in an arsenic- and iron-rich shallow-sea hydrothermal system. Geobiology. 2011; 9(5):436–45. https://doi.org/10.1111/j.1472-4669.2011.00291.x PubMed PMID: WOS:000294172100005. PMID: 21884364

37. Han Y, Perner M. The globally widespread genus Sulfurimonas: versatile energy metabolisms and adaptations to redox clines. Front Microbiol. 2015;6. https://doi.org/10.3389/fmicb.2015.00006 PMID: 25713560

38. Price RE, LaRowe DE, Italiano F, Savov I, Pichler T, Amend JP. Subsurface hydrothermal processes and the bioenergetics of chemolithoautotrophy at the shallow-sea vents off Panarea Island (Italy). Chem Geol. 2015; 407:21–45. https://doi.org/10.1016/j.chemgeo.2015.04.011 PubMed PMID: WOS:000356234100004.

39. Rogers KL, Amend JP. Archaeal diversity and geochemical energy yields in a geothermal well on Vulcano Island, Italy. Geobiology. 2005; 3(4):319–32. https://doi.org/10.1111/j.1472-4669.2006.00064.x PubMed PMID: WOS:000207172000007.

40. Rogers KL, Amend JP. Energetics of potential heterotrophic metabolisms in the marine hydrothermal system of Vulcano Island, Italy. Geochim Cosmochim Ac. 2006; 70(24):6180–200. https://doi.org/10.1016/j.gca.2006.08.046 PubMed PMID: WOS:000243166200017.

41. Amend JP, McCollom TM, Hentscher M, Bach W. Catabolic and anabolic energy for chemolithoautotrophs in deep-sea hydrothermal systems hosted in different rock types. Geochim Cosmochim Ac. 2011; 75(19):5736–48. https://doi.org/10.1016/j.gca.2011.07.041 PubMed PMID: WOS:000294479900022.

42. Boettger J, Lin HT, Cowen JP, Hentscher M, Amend JP. Energy yields from chemolithotrophic metabolisms in igneous basement of the Juan de Fuca ridge flank system. Chem Geol. 2013; 337:11–9. https://doi.org/10.1016/j.chemgeo.2012.10.053 PubMed PMID: WOS:000314738600002.

43. Dando PR, Aliani S, Arab H, Bianchi CN, Brehmer M, Cocito S, et al. Hydrothermal studies in the Aegean Sea. Phys Chem Earth PT B. 2000; 25(1):1–8. https://doi.org/10.1016/s1464-1909(99)00112-4 PubMed PMID: WOS:000084911000001.

44. Dando PR, Hughes JA, Leahy Y, Niven SJ, Taylor LJ, Smith C. Gas venting rates from submarine hydrothermal areas around the island of Milos, Hellenic Volcanic Arc. Cont Shelf Res. 1995; 15(8):913–29. https://doi.org/10.1016/0278-4343(95)80002-U PubMed PMID: WOS:A1995QM09100002.

45. Valsami-Jones E, Baltatzis E, Bailey EH, Boyce AJ, Alexander JL, Magganas A, et al. The geochemistry of fluids from an active shallow submarine hydrothermal system: Milos island, Hellenic Volcanic Arc. J Volcanol Geoth Res. 2005; 148(1–2):130–51. https://doi.org/10.1016/j.jvolgeores.2005.03.018 PubMed PMID: WOS:000233951500010.

46. Dando PR, Thomm M, Arab H, Brehmer M, Hooper LE, Jochimsen B, et al. Microbiology of shallow hydrothermal sites off Palaeochori Bay, Milos (Hellenic Volcanic Arc). Cah Biol Mar. 1998; 39(3–4):369–72. PubMed PMID: WOS:000078751400040.

47. Gilhooly WP III, Fike DA, Druschel GK, Kafantaris F-CA, Price RE, Amend JP. Sulfur and oxygen isotope insights into sulfur cycling in shallow-sea hydrothermal vents, Milos, Greece. Geochem T. 2014; 15(12). https://doi.org/10.1186/s12932-014-0012-y PubMed PMID: WOS:000341039700001. PMID: 25183951

48. Godelitsas A, Price RE, Pichler T, Amend J, Gamaletsos P, Gottlicher J. Amorphous As-sulfide precipitates from the shallow-water hydrothermal vents off Milos Island (Greece). Mar Chem. 2015; 177:687–96. https://doi.org/10.1016/j.marchem.2015.09.004 PubMed PMID: WOS:000366789100001.

49. Price RE, Savov I, Planer-Friedrich B, Buhring SI, Amend JP, Pichler T. Processes influencing extreme As enrichment in shallow-sea hydrothermal fluids of Milos Island, Greece. Chem Geol. 2013; 348:15–26. https://doi.org/10.1016/j.chemgeo.2012.06.007 PubMed PMID: WOS:000321604600003.

50. Jolivet L, Faccenna C, Huet B, Labrousse L, Le Pourhiet L, Lacombe O, et al. Aegean tectonics: Strain localisation, slab tearing and trench retreat. Tectonophysics. 2013; 597:1–33. https://doi.org/10.1016/j.tecto.2012.06.011 PubMed PMID: WOS:000320896500001.

51. Varnavas SP, Cronan DS. Submarine hydrothermal activity off Santorini and Milos in the Central Hellenic Volcanic Arc: A synthesis. Chem Geol. 2005; 224(1–3):40–54. https://doi.org/10.1016/j.chemgeo.2005.07.013 PubMed PMID: WOS:000234118800003.

52. Price RE, Lesniewski R, Nitzsche KS, Meyerdierks A, Saltikov C, Pichler T, et al. Archaeal and bacterial diversity in an arsenic-rich shallow-sea hydrothermal system undergoing phase separation. Front Microbiol. 2013; 4. https://doi.org/10.3389/fmicb.2013.00158 PubMed PMID: WOS:000331247100001. PMID: 23847597

53. Price RE, Pichler T. Distribution, speciation and bioavailability of arsenic in a shallow-water submarine hydrothermal system, Tutum Bay, Ambitle Island, PNG. Chem Geol. 2005; 224(1–3):122–35. https://doi.org/10.1016/j.chemgeo.2005.07.017

54. Bayraktarov E, Price RE, Ferdelman TG, Finster K. The pH and pCO2 dependence of sulfate reduction in shallow-sea hydrothermal CO2—venting sediments (Milos Island, Greece). Front Microbiol. 2013; 4. https://doi.org/10.3389/fmicb.2013.00111 PubMed PMID: WOS:000331102100001. PMID: 23658555

55. Helgeson HC, Kirkham DH, Flowers GC. Theoretical prediction of thermodynamic behavior of aqueous electrolytes at high pressures and temperatures: 4.Calculation of activity coefficients, osmotic

coefficients, and apparent molal and standard and relative partial molal properties to 600°C and 5 kb. American Journal of Science. 1981; 281(10):1249–516. https://doi.org/10.2475/ajs.281.10.1249 PubMed PMID: WOS:A1981MZ34200001.

56. Shock EL, Oelkers EH, Johnson JW, Sverjensky DA, Helgeson HC. Calculation of the thermodynamic properties of aqueous species at high pressures and temperatures—effective electrostatic radii, dissociation constants and standard partial molal properties to 1000°C and 5 kbar. Journal of the Chemical Society-Faraday Transactions. 1992; 88(6):803–26. https://doi.org/10.1039/ft9928800803 PubMed PMID: WOS:A1992HK65300006.

57. Tanger JC, Helgeson HC. Calculation of the thermodynamic and transport properties of aqueous species at high pressures and temperatures—revised equations of state for the standard partial molal properties of ions and electrolytes. American Journal of Science. 1988; 288(1):19–98. https://doi.org/10.2475/ajs.288.1.19. PubMed PMID: WOS:A1988L632800002.

58. Johnson JW, Oelkers EH, Helgeson HC. SUPCRT92—a software package for calculating the standard molal thermodynamic properties of minerals, gases, aqueous species, and reactions from 1 bar to 5000 bar and 0°C to 1000°C. Computers & Geosciences. 1992; 18(7):899–947. https://doi.org/10.1016/0098-3004(92)90029-q PubMed PMID: WOS:A1992JR49100006.

59. Schulte MD, Shock EL, Wood RH. The temperature dependence of the standard-state thermodynamic properties of aqueous nonelectrolytes. Geochim Cosmochim Ac. 2001; 65(21):3919–30. https://doi.org/10.1016/s0016-7037(01)00717-7 PubMed PMID: WOS:000172225600017.

60. Shock EL, Helgeson HC. Calculation of the thermodynamic and transport properties of aqueous species at high pressures and temperatures—correlation algorithms for ionic species and equation of state predictions to 5 kb and 1000°C. Geochim Cosmochim Ac. 1988; 52(8):2009–36. https://doi.org/10.1016/0016-7037(88)90181-0 PubMed PMID: WOS:A1988P889900006.

61. Shock EL, Helgeson HC. Calculation of the thermodynamic and transport properties of aqueous species at high pressures and temperatures—standard partial molal properties of organic species. Geochim Cosmochim Ac. 1990; 54(4):915–45. https://doi.org/10.1016/0016-7037(90)90429-o PubMed PMID: WOS:A1990DB65700001.

62. Shock EL, Helgeson HC, Sverjensky DA. Calculation of the thermodynamic and transport properties of aqueous species at high pressures and temperatures—standard partial molal properties of inorganic neutral species. Geochim Cosmochim Ac. 1989; 53(9):2157–83. https://doi.org/10.1016/0016-7037(89)90341-4 PubMed PMID: WOS:A1989AP91800002.

63. Sverjensky DA, Shock EL, Helgeson HC. Prediction of the thermodynamic properties of aqueous metal complexes to 1000 degrees C and 5 kb. Geochim Cosmochim Ac. 1997; 61(7):1359–412. https://doi.org/10.1016/s0016-7037(97)00009-4 PubMed PMID: WOS:A1997WV63100003.

64. Bricker O. Some stability relations in the system Mn-O2-H2O at 25° and one atmosphere total pressure. American Mineralogist. 1965; 50(9):1296-&. PubMed PMID: WOS:A19656996000009.

65. Hem JD, Roberson CE, Fournier RB. Stability of BETA-MnOOH and manganese oxide deposition from spring water. Water Resources Research. 1982; 18(3):563–70. https://doi.org/10.1029/WR018i003p00563 PubMed PMID: WOS:A1982NT27000013.

66. Helgeson HC. Thermodynamics of hydrothermal systems at elevated temperatures and pressures. American Journal of Science. 1969; 267(7):729-&. https://doi.org/10.2475/ajs.267.7.729 PubMed PMID: WOS:A1969D857000001.

67. LaRowe D, Amend J. Energetic constraints on life in marine deep sediments. In: Kallmeyer J, Wagner D, editors. Microbial Life of the Deep Biosphere. Life in Extreme Environments. 12014. p. 279–302.

68. Pehlivanoglou K. Lithology and mineralogy of surface sediments in the vicinity of the Kafireas Strait (Aegean Sea). Geo-Marine Letters. 2001; 21(2):75–85.

69. Karageorgis A, Anagnostou C, Sioulas A, Chronis G, Papathanassiou E. Sediment geochemistry and mineralogy in Milos bay, SW Kyklades, Aegean Sea, Greece. J Marine Syst. 1998; 16(3–4):269–81. https://doi.org/10.1016/s0924-7963(97)00020-1 PubMed PMID: WOS:000076604200006.

70. Sengers JL, Kamgar-Parsi B, Balfour F, Sengers J. Thermodynamic properties of steam in the critical region. Journal of Physical and Chemical Reference Data. 1983; 12(1):1–28.

71. Haar L. NBS/NRC steam tables: CRC Press; 1984.

72. Palmer M. Controls over the chloride concentration of submarine hydrothermal vent fluids: evidence from Sr/Ca and 87Sr/86Sr ratios. Earth and Planetary Science Letters. 1992; 109(1–2):37–46.

73. Albarede F, Michard A, Minster J, Michard G. 87Sr/86Sr ratios in hydrothermal waters and deposits from the East Pacific Rise at 21 N. Earth and Planetary Science Letters. 1981; 55(2):229–36.

74. de Fommervault OP, d'Ortenzio F, Mangin A, Serra R, Migon C, Claustre H, et al. Seasonal variability of nutrient concentrations in the Mediterranean Sea: Contribution of Bio-Argo floats. Journal of Geophysical Research: Oceans. 2015; 120(12):8528–50.

75. Philips S, Laanbroek HJ, Verstraete W. Origin, causes and effects of increased nitrite concentrations in aquatic environments. Reviews in environmental science and biotechnology. 2002; 1(2):115–41.

76. Garrison TS, Ellis R. Essentials of oceanography. Boston, MA: Cengage Learning; 2018. 71–3 p.

77. Giovannelli D, d'Errico G, Manini E, Yakimov M, Vetriani C. Diversity and phylogenetic analyses of bacteria from a shallow-water hydrothermal vent in Milos island (Greece). Front Microbiol. 2013; 4. https://doi.org/10.3389/fmicb.2013.00184 PubMed PMID: WOS:000331246100001. PMID: 23847607

78. Sievert SM, Heidorn T, Kuever J. Halothiobacillus kellyi sp. nov., a mesophilic, obligately chemolithoautotrophic, sulfur-oxidizing bacterium isolated from a shallow-water hydrothermal vent in the Aegean Sea, and emended description of the genus Halothiobacillus. Int J Syst Evol Micr. 2000; 50(3):1229–37.

79. Jochimsen B, Peinemann-Simon S, Völker H, Stüben D, Botz R, Stoffers P, et al. Stetteria hydrogenophila, gen. nov. and sp. nov., a novel mixotrophic sulfur-dependent crenarchaeote isolated from Milos, Greece. Extremophiles. 1997; 1(2):67–73. https://doi.org/10.1007/s007920050016 PMID: 9680304

80. Brinkhoff T, Sievert SM, Kuever J, Muyzer G. Distribution and Diversity of Sulfur-OxidizingThiomicrospira spp. at a Shallow-Water Hydrothermal Vent in the Aegean Sea (Milos, Greece). Appl Environ Microb. 1999; 65(9):3843–9.

81. Kuever J, Sievert SM, Stevens H, Brinkhoff T, Muyzer G. Microorganisms of the oxidative and reductive part of the sulphur cycle at a shallow-water hydrothermal vent in the Aegean Sea (Milos, Greece). Cah Biol Mar. 2002; 43(3/4):413–6.

82. Amend JP, LaRowe DE. Mini-Review: Demystifying Microbial Reaction Energetics. Environ Microbiol. 2019.

83. Osburn MR, LaRowe DE, Momper LM, Amend JP. Chemolithotrophy in the continental deep subsurface: Sanford Underground Research Facility (SURF), USA. Front Microbiol. 2014; 5. https://doi.org/10.3389/fmicb.2014.00610 PubMed PMID: WOS:000345698500001. PMID: 25429287

84. Houghton JL, Gilhooly WP III, Kafantaris F-CA, Druschel GK, Lu G-S, Amend JP, et al. Spatially and temporally variable sulfur cycling in shallow-sea hydrothermal vents, Milos, Greece. Mar Chem. 2019; 208:83–94.

85. LaRowe D, Amend J. Energy limits for life in the subsurface: Cambridge University Press; 2020.

86. LaRowe DE, Dale AW, Aguilera DR, L'Heureux I, Amend JP, Regnier P. Modeling microbial reaction rates in a submarine hydrothermal vent chimney wall. Geochim Cosmochim Ac. 2014; 124:72–97. https://doi.org/10.1016/j.gca.2013.09.005 PubMed PMID: WOS:000327394100005.

87. Sievert SM, Brinkhoff T, Muyzer G, Ziebis V, Kuever J. Spatial heterogeneity of bacterial populations along an environmental gradient at a shallow submarine hydrothermal vent near Milos Island (Greece). Appl Environ Microb. 1999; 65(9):3834–42.